Permeability and acoustic velocity controlling factors determined from x-ray tomography images of carbonate rocks

Nathaly L. Archilha, Roseane M. Missagia, Cathy Hollis, Marco A. R. de Ceia, Samuel A. McDonald, Irineu A. Lima Neto, David S. Eastwood, and Peter Lee

ABSTRACT

Carbonate reservoir rocks exhibit a great variability in texture that directly impacts petrophysical parameters. Many exhibit bi- and multimodal pore networks, with pores ranging from less than 1 μm to several millimeters in diameter. Furthermore, many pore systems are too large to be captured by routine core analysis, and well logs average total porosity over different volumes. Consequently, prediction of carbonate properties from seismic data and log interpretation is still a challenge. In particular, amplitude versus offset classification systems developed for clastic rocks, which are dominated by connected, intergranular, unimodal pore networks, are not applicable to carbonate rocks.

Pore geometrical parameters derived from digital image analysis (DIA) of thin sections were recently used to improve the coefficient of determination of velocity and permeability versus porosity. Although this substantially improved the coefficient of determination, no spatial information of the pore space was considered, because DIA parameters were obtained from two-dimensional analyses. Here, we propose a methodology to link local and global pore-space parameters, obtained from three-dimensional (3-D) images, to experimental physical properties of carbonate rocks to improve P-wave velocity and permeability predictions. Results show that applying a combination of porosity, microporosity, and 3-D geometrical parameters to P-wave velocity significantly improves the adjusted coefficient of determination from 0.490 to 0.962. A substantial improvement

Copyright ©2016. The American Association of Petroleum Geologists. All rights reserved. Gold Open Access. This paper is published under the terms of the CC-BY license.

Manuscript received March 17, 2015; provisional acceptance October 8, 2015; revised manuscript received December 14, 2015; final acceptance February 25, 2016.
DOI:10.1306/02251615044

AUTHORS

NATHALY L. ARCHILHA ~ *North Fluminense State University, Rodovia Amaral Peixoto, km 163, Avenida Brenand S/N, Imboassica/ 27925-310, Macaé, Rio de Janeiro, Brazil; School of Earth, Atmospheric, and Environmental Sciences, The University of Manchester, Williamson Building, Oxford Road, Manchester M13 9PL, United Kingdom; nathaly.archilha@lnls.br*

Nathaly L. Archilha is a researcher at the Brazilian Synchrotron Light Laboratory. She has a B.Sc. degree in physics from University of São Paulo and a Ph.D. in exploration and reservoir engineering from North Fluminense State University. Her research interests include carbonate porous media, x-ray tomography, and rock physics.

ROSEANE M. MISSAGIA ~ *North Fluminense State University, Rodovia Amaral Peixoto, km 163, Avenida Brenand S/N, Imboassica/ 27925-310, Macaé, Rio de Janeiro, Brazil; rose@lenep.uenf.br*

Roseane M. Missagia holds a B.Sc. degree in civil engineering from the Pontifícia Universidade Católica of Minas Gerais, and both M.Sc. degree and Ph.D. in exploration and reservoir engineering in applied geophysics from North Fluminense State University, Brazil. He is now an associate professor of petrophysics laboratory at North Fluminense State University Laboratório de Engenharia e Exploração de Petróleo. His areas of interest include rock physics modeling, seismic reservoir characterization, and seismic physical modeling.

CATHY HOLLIS ~ *School of Earth, Atmospheric, and Environmental Sciences, The University of Manchester, Williamson Building, Oxford Road, Manchester M13 9PL, United Kingdom; cathy.hollis@manchester.ac.uk*

Cathy Hollis is a reader in petrophysics and petroleum geology at The University of Manchester, United Kingdom. She has a B.Sc. degree in geological science from University of Birmingham and a Ph.D. in geology from University of Aberdeen. Her research interests are in carbonate petroleum geology,

particularly carbonate diagenesis, and petrophysics.

Marco A. R. de Ceia ~ *North Fluminense State University, Rodovia Amaral Peixoto, km 163, Avenida Brenand S/N, Imboassica/ 27925-310, Macaé, Rio de Janeiro, Brazil; marco@lenep.uenf.br*

Marco A. R. de Ceia obtained a B.Sc. degree in physics from the Rio de Janeiro Federal University, an M.Sc. degree in geophysics from Observatório Nacional, and Ph.D. in exploration and reservoir engineering from North Fluminense State University in Brazil. Since 2011, he has been an associate professor at North Fluminense State University. His main interests are in rock physics, petrophysics, and seismic physical modeling.

Samuel A. McDonald ~ *The Manchester X-ray Imaging Facility, School of Materials, The University of Manchester, Alan Turing Building, Oxford Road, Manchester M13 9PL, United Kingdom; sam.mcdonald@ manchester.ac.uk*

Samuel A. Mcdonald is a research fellow in the School of Material at The University of Manchester, United Kingdom. Previously, he completed an undergraduate degree and Ph.D. in material science at The University of Manchester, United Kingdom. His research interests are in x-ray tomography application to study in situ deformation and damage of granular materials due to high strains-rate loadings.

Irineu A. Lima Neto ~ *North Fluminense State University, Rodovia Amaral Peixoto, km 163, Avenida Brenand S/N, Imboassica/ 27925-310, Macaé, Rio de Janeiro, Brazil; irineu@gmail.com*

Irineu A. Lima Neto received his B.Sc. degree in computer science (2005), and both M.Sc. degree and Ph.D. in exploration and reservoir engineering from North Fluminense State University, in 2008 and 2015, respectively. Currently, he is a researcher at North Fluminense State University/FUNDENOR (Regional Development Foundation). His main interests in the geoscience area range from digital image analysis to rock physics characterization.

David S. Eastwood ~ *The Manchester X-Ray Imaging Facility, Research Complex at*

is also observed in permeability prediction (from 0.668 to 0.948). Both results can be interpreted to reflect a pore geometrical control and pore size control on P-wave velocity and permeability.

INTRODUCTION

A large fraction of the world's hydrocarbons is reservoired in carbonate rocks, including the supergiant fields in the Middle East and the recent discoveries of the presalt region, offshore Brazil. Carbonate rocks are highly prone to postdepositional alteration, such as dissolution and cementation, and these processes modify the pore structure, creating or destroying porosity and changing permeability and acoustic properties (Rafavich et al., 1984; Anselmetti et al., 1998; Eberli et al., 2003; Weger et al., 2009; Hollis et al., 2010; Castro and Rocha, 2013).

Eberli et al. (2003) showed that total porosity and pore type have nearly the same impact on the acoustic behavior of carbonate rocks and that the most used velocity–porosity empirical relations—for example, Gardner (Raymer et al., 1980) and Wyllie (Wyllie et al., 1958)—do not predict velocity with a high coefficient of determination (R^2). A clear understanding of the relationship between sonic velocity and porosity is therefore fundamental to the prediction of pore volume from acoustic data. Importantly, the most widely used algorithms for seismic inversion and log interpretation do not consider pore-shape factors, and, consequently, they can significantly over- or underestimate hydrocarbon volumes.

Weger et al. (2009) introduced the digital image analysis (DIA) method to improve the prediction of velocity and permeability. The study used two-dimensional (2-D) images from thin section, and a good improvement in velocity prediction was observed, with the R^2 increasing from 0.542 to 0.845. Permeability estimation was also greatly improved, although the highest R^2 value showed a weak relationship ($R^2 < 0.5$) between the DIA parameters, permeability and porosity.

Carbonate rocks usually present a wide range of permeability for the same porosity value because of a marked variability in the connectivity of pores, both with respect to average coordination number (the number of neighboring pores) and pore-throat diameter (Lucia, 2007; Ahr, 2008; Hollis et al., 2010; Jivkov et al., 2013). Raoof and Hassanizadeh (2012) showed the importance of including the coordination number to estimate the permeability. Later, Jivkov et al. (2013) demonstrated that the coordination number is a more important control parameter on permeability than total porosity. However, the pore geometry, pore-throat radius, and coordination number cannot be reliably quantified using thin-section images, because three-dimensional (3-D) information cannot be

assessed. Furthermore, although conventional measurements of capillary pressure can be used to determine pore-throat diameter, they do not provide spatial information on the distribution of those pore throats nor the coordination number. However, 3-D images from x-ray tomography can be used to determine these parameters and also to visualize the pore and matrix structures. In this study, we show how information regarding pore space, obtained by x-ray tomography, can improve the prediction of acoustic properties and absolute permeability for a suite of Albian carbonate rocks from two neighboring offshore wells from the postsalt region of Campos Basin, Brazil. We extract the pore shape, size, and volume; tortuosity (τ); and coordination number from 3-D images of the pore space and incorporate this information into established models, such as Kozeny (1927) for permeability estimation and Kuster and Toksöz (1974a, b) for velocity prediction.

RESERVOIR GEOLOGY

The Campos Basin (Figure 1) is the major petroleum basin in Brazil. It is located in the southeastern part of the country and hosts more than 50 oilfields, which produced almost 1.8 million bbl/day of oil and natural gas in 2013 (Agência Nacional do Petróleo, 2014). These oilfields are located 50 to 140 km (31.1–87.0 mi) offshore of Brazil, and the water depth ranges from 80 to 2400 m (0.05–1.5 mi).

Key reservoirs are Cretaceous (Barremian, early Albian, and late Albian) to early Miocene in age. For this study, a suite of postsalt, Cretaceous (Albian) carbonates from two neighboring wells (W1 and W2) within the Campos Basin were studied. They form reserves in shallow water (<200 m [0.12 mi]) at burial depths of less than 1 km (0.62 mi) and are composed mostly of grainstones and packstones containing oncolites, peloids, oolites, and bioclasts. This study focused on oolitic grainstones and cemented grainstones.

Oncolite and oolite-rich skeletal grainstones and clean packstones comprise the best-quality reservoir facies, with porosity ranging from 20% to 34% and permeability usually greater than 100 and up to 2000 md (Bruhn et al., 2003). The samples comprise more than 95% calcium carbonate with minor (<2%) detrital quartz, dolomite, and rare feldspar.

Typically, oncolitic and oolitic peloidal grainstones are moderately to poorly sorted (see Figures 2 and 3 for supporting images and Table 1 for thin-section description). Skeletal and nonskeletal allochems are highly micritized and exhibit a thin, discontinuous, grain-rimming cement. Macroporosity (ϕ_{CT}) is dominated by primary interparticle macropores, supplemented by secondary intraparticle macropores, biomolds, and vugs. Mechanical compaction is usually moderate, with common point contacts, and

Harwell and Diamond Light Source, School of Materials, The University of Manchester, Alan Turing Building, Oxford Road, Manchester M13 9PL, United Kingdom; david.eastwood@manchester.ac.uk

David S. Eastwood is a research associate in the School of Materials at The University of Manchester, United Kingdom specializing in x-ray imaging. He is based at Diamond Light Source, the United Kingdom Synchrotron, and previously completed an undergraduate degree and Ph.D. in physics at the University of Durham, United Kingdom.

PETER LEE ~ *The Manchester X-Ray Imaging Facility, Research Complex at Harwell and Diamond Light Source, The University of Manchester, Alan Turing Building, Oxford Road, Manchester M13 9PL, United Kingdom; peter.lee@manchester.ac.uk*

Peter Lee is a professor of materials imaging in the School of Materials at The University of Manchester. He leads a group of 30 researchers developing innovative synchrotron x-ray imaging techniques. These novel techniques are applied to elucidate new insights into materials, geological, and biological challenges.

ACKNOWLEDGMENTS

The authors thank Agência Nacional do Petróleo and Petrobras for providing the rock samples; North Fluminense State University, Brazil, for the facilities to perform part of this work; and Henry Moseley Imaging Facility (The University of Manchester) and the Diamond–Manchester Collaboration for the award of beamtime (MT4017-1) for experimental measurements of x-ray tomography. We also acknowledge the facilities provided by the Research Complex at Harwell, funded in part by the Engineering and Physical Sciences Research Council (EP/I02249X/1). Nathaly L. Archilha thanks the Coordenação de Aperfeiçoamento de Pessoal de Nível Superior, within the Ministry of Education of Brazil, and the Science without Borders program for the scholarship.

EDITOR'S NOTE

Color versions of Figures 1–13 can be seen in the online version of this paper.

often elongated grain contacts, although dissolution is rare and stylolites are absent.

Cemented grainstones comprise fine-grained peloidal foraminiferal grainstones and clean packstones, with coarse-grained oncoliths and skeletal allochems (bivalves and gastropods) in places. In these samples, the primary interparticle ϕ_{CT} is occluded by very finely crystalline sparry calcite and syntaxial overgrowths on echinoderm debris. The ϕ_{CT} is restricted to rare, small biomolds. One sample (W2-03) is a muddy packstone, which comprises significantly less pore-filling cementation and greater compaction than the other samples.

EXPERIMENTAL METHODS

Petrophysical Measurements

Measurements of total porosity were conducted on 3.8-cm (1.5-in.) plugs using a helium porosimeter and were repeated six times. An average value was

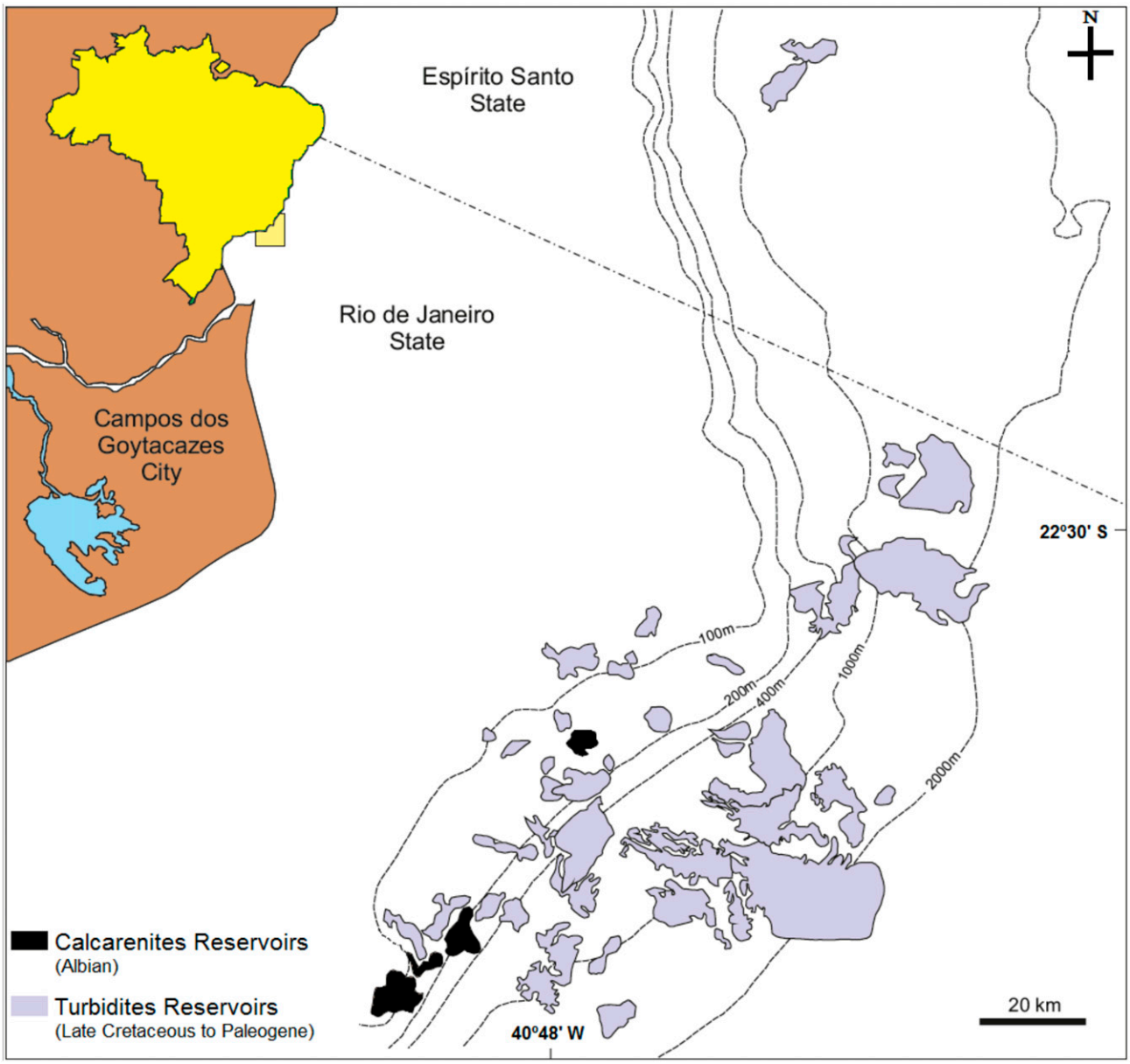

Figure 1. Location map of the Campos Basin (modified from Bruhn et al., 2003).

determined, and a standard deviation of less than 5% was achieved.

Permeability measurements were conducted on the same samples using a gas permeameter. The gas flow rate (q), outlet pressure (P_0), and inlet pressure (P_i) were measured at least 10 times for each sample, and the permeability was determined using Darcy's law for gases:

$$q = \frac{kA}{2000\upsilon L}\frac{\left|P_0^2 - P_i^2\right|}{P_{\text{atm}}} \quad (1)$$

where k is the permeability; υ is the fluid viscosity; L and A are, respectively, the length and the cross sectional area of the sample; and P_{atm} is the atmospheric pressure.

Mercury intrusion porosimetry (MIP) measurements were conducted on small pieces of approximately 0.5 cm (~0.2 in.) sample edges, and they were only permitted for two samples (W1-02 and W2-03) to limit the destruction of core material. The MIP provided the range of the pore-throat diameter, which was used to determine the best computerized tomography (CT) scanner to analyze the rocks and for further correlation with pore diameter.

X-Ray Diffraction and Rietveld Method

X-ray diffraction (XRD) analysis and interpretation using the Rietveld method (Rietveld, 1969) was used to quantify the mineralogy of the rocks. This method makes it possible to adjust different XRD patterns; refine parameters related to sample physical characteristics (size and grain microstrain), structural parameters (position and atomic displacement), and instrumental parameters (background radiation, wavelength, slit, etc.); and obtain the best fit between the experimental measurement and the adjusted equation.

A piece of dried rock was disaggregated in an agate mortar and passed through a 60-μm sieve to ensure the best-quality measurement. A fast detector x-ray diffractometer was set up to work at 30 kV and 10 mA; the step angle was 0.02°, and the scanning rate was 0.6 s/step. A 0.6-mm knife edge was used to reduce the effective reflecting area. The quantitative analysis was made with the General Structure Analysis System software for Rietveld analysis (Larson and Von Dreele, 2004), and the difference between the measured and the adjusted curves was less than 3% for all cases. The mineralogy information was used to characterize the rock and estimate the P-wave velocity (V_p) of the mineral matrix.

Acoustic Property Measurements

Ultrasonic V_p measurements were conducted at North Fluminense State University (Macaé, Brazil) on room-dried plugs (3.8 cm [~1.5 in.] in diameter, 5.1 cm [~2 in.] in length) using a hydrostatic pressure vessel set up to work at an effective pressure of 2.5 MPa and a pore pressure of 0.1 MPa (ambient pressure). The experimental error for velocities is approximately 1% (for detailed experimental information, see Lima Neto et al., 2014).

X-Ray–Computed Microtomography

X-ray tomography is a nondestructive method that uses x-rays to produce tomographic images of a

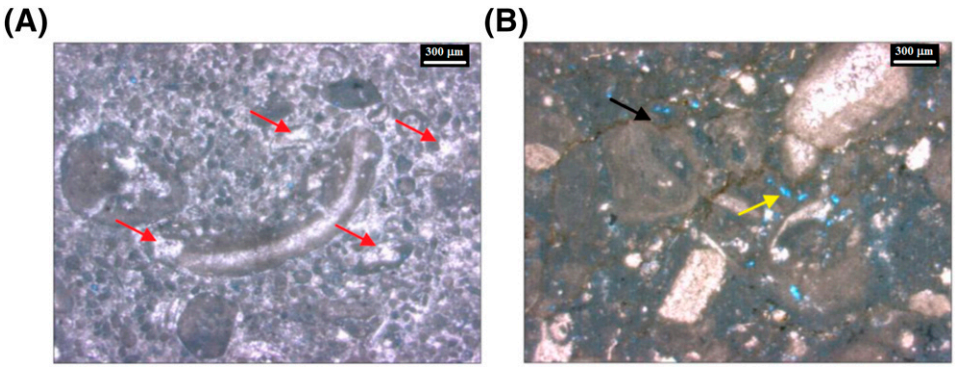

Figure 2. Thin-section photomicrograph images of analyzed samples: (A) W2-01 (porosity [ϕ] = 16.3%, permeability [k] = 0.24 md, P-wave velocity [V_p] = 4.11 km/s [13,484 ft/s]), poorly sorted oncolitic peloidal skeletal packstone–grainstone in which interparticle and intraparticle macroporosity are pervasively calcite cemented (red arrows), and (B) W2-03 (ϕ = 21.9%, k = 2.02 md, V_p = 2.64 km/s [8661 ft/s]), poorly sorted oncolitic peloidal skeletal packstone with isolated biomolds (yellow arrow) and compaction seams (black arrow). Note: A color version can be seen in the online version.

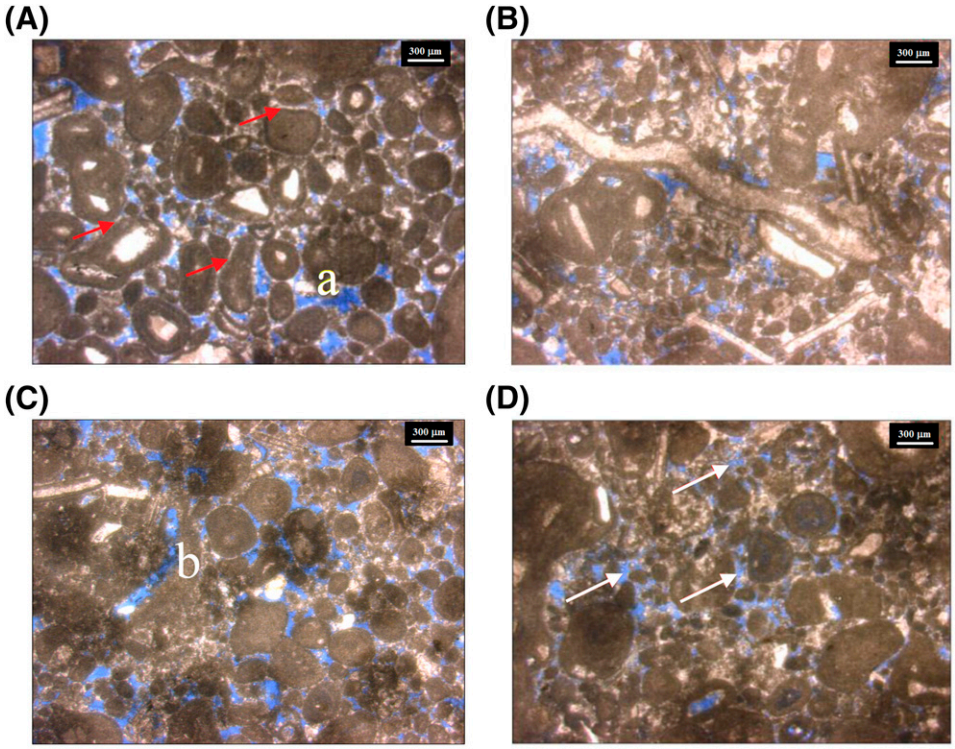

Figure 3. Thin-section photomicrograph images of analyzed samples: (A) W1-01 (porosity [ϕ] = 23.0%, permeability (k) = 8.95 md, P-wave velocity [V_p] = 3.11 km/s [10,203 ft/s]), moderately sorted oolitic and oncoidal skeletal grainstone within thin grain-rimming cement (red arrows [in color version]) and primary interparticle macropores (e.g., a); (B) W1-02 (ϕ = 25.7%, k = 222 md, V_p = 2.97 km/s [9744 ft/s]), moderately sorted oolitic skeletal grainstone with patchy calcite cement; (C) W1-05 (ϕ = 28.9%, k = 602 md, V_p = 2.26 km/s [7415 ft/s]), moderately well-sorted peloidal skeletal grainstone with primary interparticle macropores supplemented by biomolds (b); and (D) W1-07 (ϕ = 22.9%, k = 9.78 md, V_p = 2.84 km/s [9318 ft/s]), poorly sorted oncolitic peloidal skeletal grainstone in which the primary interparticle pore network has been solution enhanced (white arrows).

scanned sample; this allows the structures inside the sample to be studied without cutting it. The process involves rotation of a sample in an x-ray beamline while the detector collects the projections (radiographs) for each angle. A scintillator positioned between the sample and the detector transforms x-rays into visible light. Thereafter, reconstruction algorithms are used to generate a 3-D image of the sample from the radiographic images.

Cubic samples with 2-mm-long edges were prepared with a wire saw and scanned using two systems: Xradia MicroXCT at The University of Manchester and the high-resolution beamline I13 at Diamond Light Source (Oxford, United Kingdom). For all the samples, the Xradia scanner was set up to work at 90 keV and 111 µA; the magnification was 9.8×, and the pixel size was 1.1 µm. For the I13, the x-ray energy was monochromated to 22 keV, and 1800 projections over a 180° rotation were captured with an exposure time of 6 s each. The pixel size was 1.125 µm. The samples did not exceed the field of view, and the scan time for each sample was approximately 12 hr on the Xradia and approximately 4 hr on the I13. Avizo Fire 8.1, a 3-D visualization software program (FEI, 2015), and an extension package (XSkeleton) were used for data filtering, segmentation, and analysis.

Local and Global Parameters

From a 3-D image, it is possible to obtain global and local parameters. Global parameters are related to the overall pore-space properties, such as microporosity (ϕ_μ), macroporosity (ϕ_{CT}), specific surface area (SSA), and tortuosity (τ), whereas the local parameters are associated with properties of a single pore. These are mostly related to the specific properties of the pore, such as geometry, aspect ratio (AR), and roundness. The following parameters were collected.

- The SSA: the ratio of total pore surface area to total pore volume. Usually, a small number (<200 mm^{-1} [7.87 in.$^{-1}$]) indicates a simple geometry. In this study, SSA values range from 164 mm^{-1} (6.46 in.$^{-1}$) for oolitic grainstones to 721 mm^{-1} (23.38 in.$^{-1}$) for cemented grainstones.

Table 1. Texture and Thin-Section Description for All Samples

Samples	Texture	Thin-Section Descriptions
W1-01	OG	Poorly sorted oolitic and oncoidal skeletal grainstone to clean packstone with fine-grained peloids. Weak grain-fringing cement, point and elongate grain contacts, recrystallized micrite. Primary macroporosity, vugs, and rare biomolds.
W1-02	OG	Moderately sorted oolitic skeletal grainstone with fine-grained peloids. Grain-fringing cement—thin but usually completely coats grains. Primary macroporosity and vugs.
W1-03	OG	Poorly sorted peloidal skeletal grainstone to clean packstone with fine-grained peloids. Weak grain-fringing cement and localized patchy pore-filling calcite. Primary macroporosity and rare biomolds and vugs.
W1-04	OG	Poorly sorted oolitic skeletal grainstone to clean packstone with fine-grained peloids and benthic foraminifera. Weak grain-fringing cement and localized patchy pore-filling calcite. Primary macroporosity and rare biomolds and vugs.
W1-05	OG	Moderately well-sorted peloidal skeletal grainstone to clean packstone with fine-grained peloids and some coarser oncoliths and rare ooids. Weak grain-fringing cement and localized patchy pore-filling calcite. Primary macroporosity and rare vugs.
W1-06	OG	Moderately well-sorted peloidal skeletal grainstone to clean packstone with fine-grained peloids and some coarser oncoliths and rare ooids. Weak grain-fringing cement and localized patchy pore-filling calcite. Primary macroporosity and rare vugs.
W1-07	OG	Poorly sorted oncolitic peloidal skeletal grainstone to clean packstone with fine-grained peloids. Weak grain-fringing cement and pore-filling calcite. Primary macroporosity and rare vugs and biomolds.
W2-01	CG	Poorly sorted oncolithic peloidal skeletal grainstone to clean packstone with fine-grained peloids and benthic foraminifera. Weak grain-fringing cement and pore-filling calcite. Rare, small, isolated biomolds.
W2-02	CG	Fine-grained peloidal packstone with fine-grained skeletal allochems. Patchy pore-occluding calcite and syntaxial overgrowths. Very small primary interparticle macropores and rare, isolated biomolds.
W2-03	CG	Poorly sorted oncolitic peloidal skeletal packstone with fine-grained peloids and benthic foraminifera. Patchy pore-occluding calcite and syntaxial overgrowths compacted. Minor, isolated biomolds.
W2-04	CG	Fine-grained peloidal foraminiferal grainstone to clean packstone with large oncoliths and skeletal allochems. Pervasive pore-occluding calcite and syntaxial overgrowths. Minor, isolated biomolds.

Abbreviations: CG = cemented grainstone; OG = oolitic grainstone.

- Dominant pore size (DomSize): the upper boundary of the pore radius, of which 50% of the porosity on a 3-D image is composed; it represents the pore radius that dominates the sample. This property is determined by the equivalent spherical diameter of each irregular pore (i.e., the diameter of a sphere of equivalent volume). In this study, DomSize ranges from 9.2 μm for cemented grainstones to 76.7 μm for oolitic grainstones.
- Gamma (γ): defined for 2-D images as the ratio of the perimeter to the area (perimeter over area) for a single pore normalized to a circle (Anselmetti et al., 1998). In this study, we reformulated this parameter for 3-D images. The new γ is now defined as the SSA of a single pore normalized to a sphere, as shown in equation 2, where A_S is the surface area and V is the pore volume. It describes the sphericity of the pore, and, in our data, the area-weighted mean value of γ (considering the entire imaged pore space) ranges from 1.28 to 2.14. A γ value close to 1 indicates that the pore is spherical, whereas a larger number indicates that the pore is flattened.

$$\gamma = \frac{2}{3}\frac{\sqrt{A_S \pi}}{\sqrt[3]{\frac{16}{9}\pi^2 V}} \tag{2}$$

- AR: the ratio of the minor (a) to major (b) lengths of the pore (Figure 4). The AR for an individual pore ranges from approximately 0.1 to approximately 1 (Figure 5), and the average AR of macropores in this study ranges from 0.54 and 0.59, with no significant variation between oolitic and cemented grainstone.
- Microporosity (ϕ_μ): the difference between the gas porosity, measured on a core plug (ϕ_{gas}), and the visible porosity (i.e., ϕ_{CT}) obtained from the 3-D image of the sample (equation 3). For this estimation, we assume that the imaged pore space of the rock is representative of the whole plug.

$$\phi_\mu = \phi_{gas} - \phi_{CT} \tag{3}$$

- τ: the ratio of the length of the path of the fluid inside the rock to the straight distance between its end points (i.e., the length of the sample). It was calculated using the Centroid Path Tortuosity function (as defined in Avizo Fire). This module first computes the centroid of each 2-D image, then computes the path length through the centroids, and then divides the path length by the number of planes multiplied by the resolution along the axis.
- Coordination number: the number of pore throats connected to one pore. The average coordination number, which is used in this study, is defined as the ratio of the total number of pore throats to the number of pores in the sample. In this work, we created and analyzed the centerline tree (Figure 6A), which is the skeleton of the pore space, where each segment represents a pore, and nodes represent either the pore throats (junctions) or the pore edge. Because the software does not differentiate pore throats and edges, the highest possible value is 2, which is the isolated pore case (two nodes and one segment). Increasing the number of connections decreases the coordination number, as shown if Figure 6, where Figure 6B is the isolated pore case; Figure 6C represents two connected pores, with a coordination number of 3/2; and Figure 6D shows three connected pores and a coordination number of 4/3. Although this methodology does not provide coordination-number values commonly reported in literature, which range from 6 to approximately 40 (Matthews and Spearing, 1992; Ioannidis and Chatzis, 1993; Reeves and Celia, 1996; Raoof and Hassanizadeh, 2012; Jivkov et al., 2013), it does differentiate the connecticity of the pore space, which is sufficient for this study. In this work, the coordination number ranges from 1.36 to 1.99.

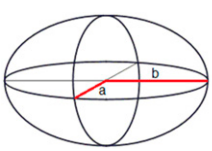

$$\alpha = \frac{a}{b};\ if\ \begin{cases} b = a \rightarrow \alpha = 1 & (sphere) \\ b >> a \rightarrow \alpha \approx 0 & (crack) \\ b > a \rightarrow 0 < \alpha < 1 & (ellipsoid) \end{cases}$$

Figure 4. Representation of the aspect ratio of a single pore. α = aspect ratio; a = minor length of the pore; b = major length of the pore.

Prior to the pore-space analysis, the raw image was preprocessed; the region of interest was cropped, a median filter was applied, and the image was segmented into pores and matrix. This created an image

where the grains were represented by rounded elements and the pores were represented by elements without a definite shape (Figure 7A). All of the global parameters were extracted from this image, whereas local parameters were obtained from images such as Figure 7B, where the total pore space was separated into individual pores, with each color representing a different pore (in the color version). Figure 7C shows a 3-D rendering of this pore space.

Rock-Physics Model: Determination of Acoustic Properties

Bulk (K) and shear (μ) modulus are rock properties related to the rock's rigidity and can be estimated by rock-physics models; this estimation enables P- and S-wave velocity prediction. The Kuster and Toksöz (KT) model, for example, derives expressions for acoustic velocities from the long-wavelength scattering theory, and, because it considers isolated pores, this approach simulates very-high-frequency rock behavior, appropriate to ultrasonic laboratory conditions. The equations 4 and 5 show the effective moduli K_{KT} and μ_{KT}, where the coefficients Z and Q describe the effect of an arbitrary inclusion (i) in a background medium (m) and are given by equations 6 and 7. The tensors T_{iijj} and T_{ijij} relate the uniform far-field strain to the strain field within the ellipsoidal inclusion (Wu, 1966) and are expressed in terms of the AR of each inclusion. Finally, the summation is over all the N inclusion types with its volume concentration (x_i). For the complete tensor mathematical formulation, see Berryman (1980) and Mavko et al. (2009).

$$(K_{KT} - K_m)\frac{\left(K_m + \frac{4}{3}\mu_m\right)}{\left(K_{KT} + \frac{4}{3}\mu_m\right)} = \sum_{i=1}^{N} x_i(K_i - K_m)Z \quad (4)$$

$$(\mu_{KT} - \mu_m)\frac{(\mu_m + \varsigma_m)}{(\mu_{KT} + \varsigma_m)} = \sum_{i=1}^{N} x_i(\mu_i - \mu_m)Q \quad (5)$$

$$\text{with} \quad \varsigma_m = \frac{\mu_m}{6}\frac{(9K + 8\mu)}{(K + 2\mu)}$$

$$PZ = \frac{1}{3}T_{iijj} \quad (6)$$

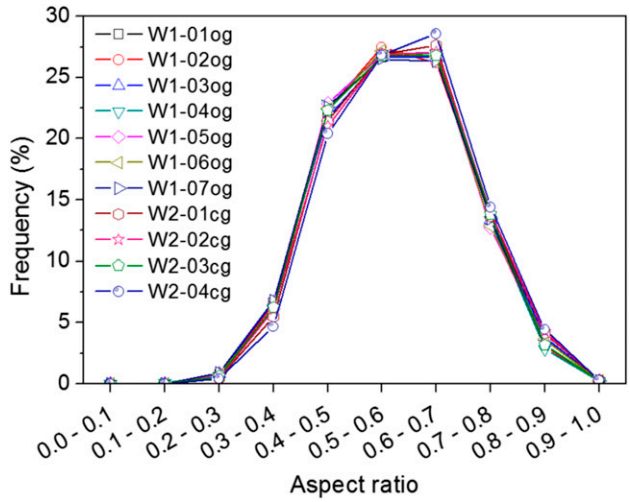

Figure 5. Aspect-ratio distribution for all the studied samples. cg = cemented grainstone; og = oolitic grainstone.

$$Q = \frac{1}{5}\left(T_{ijij} - \frac{1}{3}T_{iijj}\right) \quad (7)$$

The initial model parameters were obtained from the experimental measurements, except for the microporosity AR. Because this geometric property is not uniquely determined, microporosity AR can be considered a convenient free parameter to better fit the observation (Xu and White, 1995; Keys and Xu, 2002; Pratson et al., 2003; Lee, 2008), as long as the estimated elastic moduli are within the upper and lower Hashin–Shtrikman bounds (Zhang and Stewart, 2008).

Many authors (Sayers, 2008; Li and Zhang, 2010; Wang and Sun, 2010) indicate that microporosity AR ranges from 0.01 to 0.5 and is usually less than 0.2. Typically, a low AR, close to 0.01, is adopted for high-pressure situations. However, in this work, because the effective pressure is null (ambient pressure on CT scans) or very low (2.5 MPa on ultrasonic measurements), AR is fixed at 0.1, because a sensitivity test showed that this AR led to the best fit between the estimated (V_{pKT}) and measured P-wave velocities. Figure 8 shows a crossplot between these two properties.

Kozeny's Equation: Determination of Permeability

The Kozeny equation (equation 8) is one of the most popular and fundamental correlations between permeability and porosity (Kozeny, 1927). It was derived

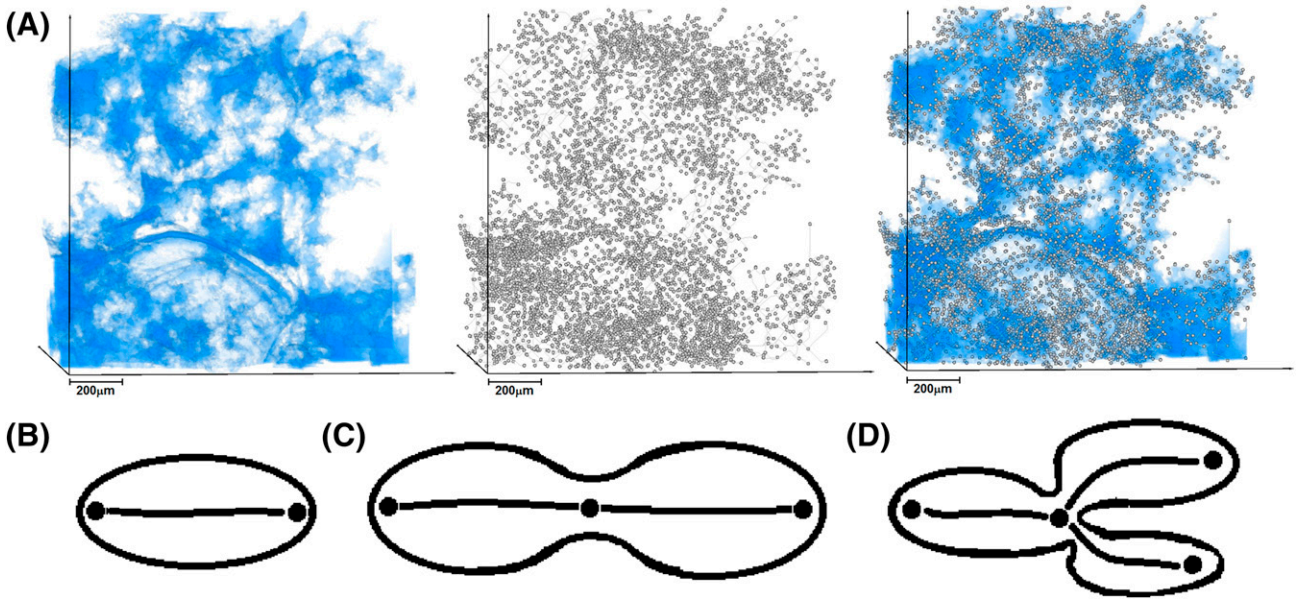

Figure 6. (A) Centerline tree (in gray) representing the pore space (in blue) of a rock, created from a binary image. The spherical blue structure in the bottom left corner is a single pore created by shell dissolution; (B) a single isolated pore; (C) two connected pores, with a coordination number of 3/2; and (D) three connected pores with a coordination number of 4/3. Note: A color version can be seen in the online version.

from a rock model where the pore space was described as n capillary tubes, with the space between these tubes filled with a nonporous material. Later, Mortensen et al. (1998) redefined this equation, introduced the Kozeny factor (c), and expressed the permeability (k) in terms of this parameter, porosity (ϕ), and SSA (S), as shown in equation 9. Variable c ranges from 0.15 to 0.25 as the porosity increases from 5% to 50% (Mortensen et al., 1998).

$$k = \frac{c\phi^3}{S^2} \tag{8}$$

$$c = \left(4\cos\left[\frac{1}{3}\arccos\left\{\phi\frac{64}{\pi^3} - 1\right\} + \frac{4}{3}\pi\right] + 4\right)^{-1} \tag{9}$$

Figure 9 shows a crossplot between estimated (k_K) and measured permeability. Despite the reasonable adjusted R^2 (0.668), the model has a tendency to overestimate low permeabilities (<100 md) and underestimate high permeabilities (>100 md).

Statistical Model and Multiple Linear Regressions

To try to improve the R^2, P-wave velocities estimated by KT ($V_{p\mathrm{KT}}$) and permeability derived from Kozeny's equation (k_K) were combined with global and local geometrical parameters of the pore space by using multiple linear regressions (MLRs). The proposed model is described in equation 10, where P_m is the measured property, P_e represents the estimated property, X_n represents global and local parameters, and β_n are coefficients determined by the regression.

$$P_m = \beta + \beta_0 P_e + \beta_1 X_1 + \beta_2 X_2 + \ldots \tag{10}$$

This study focused on determining how this statistical model fits to the experimental data by analyzing the adjusted coefficient of determination ($\overline{R}^2$) estimated by equation 11, where n is the sample size, and p is the total number of variables in the linear model. Unlike the R^2, $\overline{R}^2$ increases when a new independent variable is included only if it improves R^2 more than expected by chance, because it considers the degree of freedom of the data set.

$$\overline{R}^2 = 1 - \left(1 - R^2\right)\frac{n-1}{n-p-1} \tag{11}$$

In an MLR, the sample size must be large enough to ensure stable model coefficients. If the sample size is inadequate, the model may not generalize well beyond the current sample (Brooks and Barcikowski, 2012). To provide minimal shrinkage of the R^2, many authors state rules to determine the sample size,

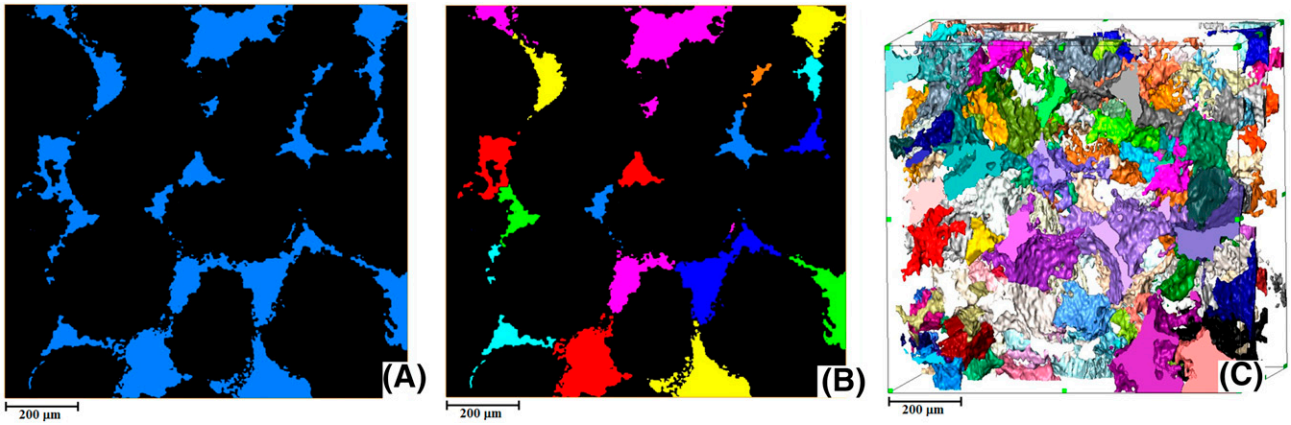

Figure 7. (A) Binary image representing the pore space (blue) and the matrix (black); (B) the separated pore space, where each color represents a different pore (color repetition occurs because of the large amount of pores); (C) tridimensional representation of the separated pore space. Note: A color version can be seen in the online version.

but they are normally inconsistent with each other (Knofczynski and Mundfrom, 2008). The ratio of sample size to predictors ranges widely, from 30 to 1 (Pedhazur and Schmelkin, 1991) to 10 to 1 (Miller and Kunce, 1973). This study was developed with only 11 samples, mainly because of the high cost and time required for imaging the samples and processing the data. Clearly, this ratio is below that expected to describe the whole reservoir, and, for this reason, all the results obtained here reflect the behavior of this set of data only. Nevertheless, the workflow presented in this study can be applied to a larger data set. As reported by Brooks and Barcikowski (2012), a study with an insufficient sample size is likely to commit type I and II statistical errors. A type I error is the incorrect rejection of a true null hypothesis (a "false positive"), and a type II error is the failure to reject a false null hypothesis (a "false negative"). For this reason, in addition to adjusted R^2 determination, p-value and statistical power were calculated for each MLR. A low p-value (<0.05) and a high statistical power (>0.8) indicate that there is a low probability that these errors were committed in the MLR.

RESULTS: P-WAVE VELOCITY AND PORE-SPACE PARAMETERS

Figure 10 shows the inverse relationship between velocity and porosity for the sample set. Although these data show a good correlation (R^2 = 0.663), there are important deviations from this trend, where lower porosity samples have comparably slower than predicted velocities (sample W2-03—solid arrow) and higher porosity samples have relatively higher than predicted velocities (sample W1-02—dashed arrow). Because these samples have the same mineralogy, as presented in Table 2, and experiments were conducted on dry samples, this is interpreted to reflect a pore topological control on acoustic properties.

Petrographical and 3-D image analysis (Tables 3 and 4) reveal that the lowest porosity sample, W2-01 (Figure 2; 16.3%), has the fastest velocity (V_p = 4.11 km/s [13,484 ft/s]) and the lowest permeability (0.24 md). Correspondingly, it has the lowest volume of ϕ_{CT} (1.44%), smallest DomSize (12.2 µm), highest SSA (721 mm^{-1}), and largest coordination number (1.99). Conversely, the sample with the highest total porosity (28.89%), W1-05 (Figure 3), has the highest permeability (602 md) and slowest velocity (V_p = 2.26 km/s [7415 ft/s]). Interestingly, it does not have the highest volume of ϕ_{CT} (10.61%, compared with a maximum of 11.50% in sample W1-02), the largest DomSize (64.92 µm, compared with a maximum of 76.7 µm in sample W1-02), or the lowest SSA (176 mm^{-1} compared with a minimum of 163 mm^{-1} in sample W1-02).

Two outlier points are identified in Figure 10. Sample W2-03 (solid arrow) has a slower than expected velocity (2.64 km/s [8661 ft/s]) for its measured porosity (19.7%). This sample is a poorly sorted onocolitic peloidal skeletal packstone (Figure 2) and the sample with the highest volume of micrite in the data set. Consequently, it has undergone more compaction than other samples, as evidenced by

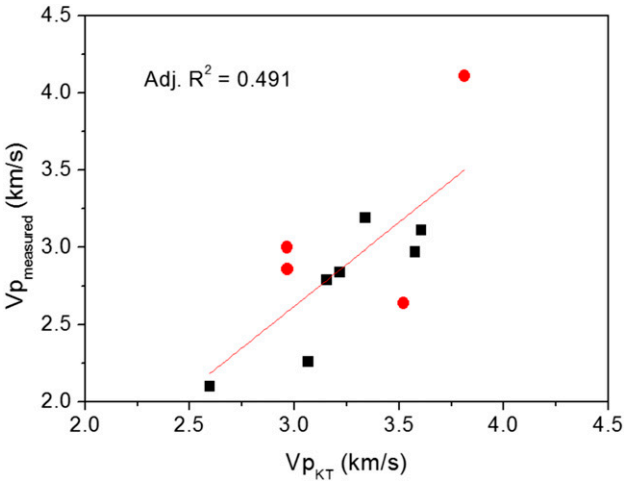

Figure 8. Crossplot between measured ($V_{pmeasured}$) and estimated (Vp_{KT}) velocities. Cemented grainstones are represented by circles and oolitic grainstones by squares. Adj. R^2 = adjusted coefficient of determination.

discontinuous, wispy microstylolites. No primary ϕ_{CT} is seen, but small, isolated biomolds are preserved. It has the highest γ of all the samples (2.14), but compared with other samples from this well (W2), it has the highest volume of ϕ_{CT} (3.01%), largest DomSize (19.31 μm), and lowest SSA (516 mm^{-1}). In contrast, sample W1-02 (Figure 3) has a faster velocity (2.97 km/s [9744 ft/s]) than would be expected for its porosity (25.7%). This sample is a moderately well-sorted oolitic skeletal grainstone with most grains exhibiting a thin, but continuous, grain-rimming cement and has an excellent permeability (222 md). Compaction is relatively minor and typically manifests as point contacts. The primary macropore network is well preserved and supplemented by vugs. This sample has the highest volume of ϕ_{CT} (11.5%), largest DomSize (76.7 μm), and lowest SSA (163 mm^{-1}) of the data set.

Therefore, qualitatively, there appears to be a broad relationship between velocity and total porosity and between permeability and porosity. In general, there is a corresponding decrease in ϕ_{CT} and ϕ_{μ}, a slight decrease in γ and an increase in SSA as velocity increases. As permeability increases, ϕ_{CT} and DomSize also increase, whereas SSA, coordination number, and τ decrease (see the Appendix, Figures 14–24, for the most important crossplots). In addition, a direct relation between DomSize (from x-ray CT) and average pore-throat diameter (from MIP) was observed. Figure 11 shows the pore-throat diameters and their fractions for sample W1-02 and W2-03. Sample W1-02, which is an oolitic grainstone, has a DomSize of 76.7 μm and an average pore-throat diameter of 1.06 μm, compared with W2-03, a cemented grainstone with a DomSize of 19.3 μm and an average pore-throat diameter of 0.51 μm.

Nevertheless, the data set reveals anomalies, which are apparently related to complexities in the pore geometry induced by compaction. Where grain-fringing cements completely coat allochems within the well-sorted, clean grainstone, compaction is inhibited and ϕ_{CT} is preserved. Sample W1-02 has the lowest volume of ϕ_{μ} (55.2% of the total pore volume) of all samples. In comparison, the most micritic, least well-sorted sample (W2-03) is highly compacted and has a slower velocity than expected for its total measured porosity. Because this sample is not the most microporous sample in the data set (84.7% of total porosity is ϕ_{μ}, compared with 96.9% in sample W2-02) and does not have the highest SSA or smallest DomSize, it is difficult to constrain the key control on velocity and permeability. This suggests that there is not a single parameter that controls the measured properties; multiple controls must be operating, and these cannot be fully determined by geological observation alone.

To improve the velocity and permeability estimation, MLR was used to examine the link of velocity

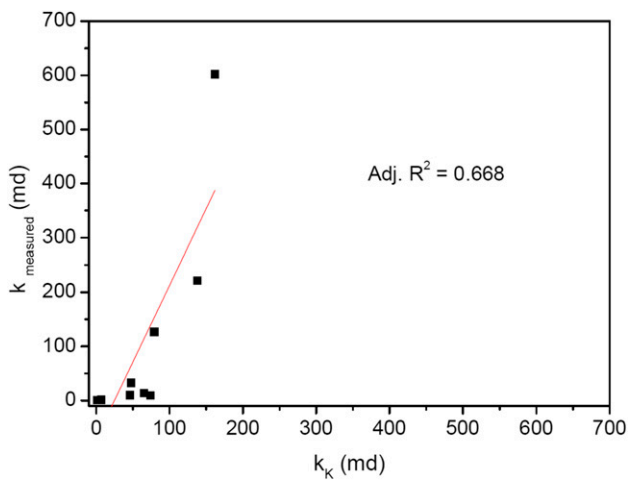

Figure 9. Crossplot between Kozeny estimation (k_k) and gas ($k_{measured}$) permeability. Cemented grainstones are represented by circles and oolitic grainstones by squares. Adj. R^2 = adjusted coefficient of determination.

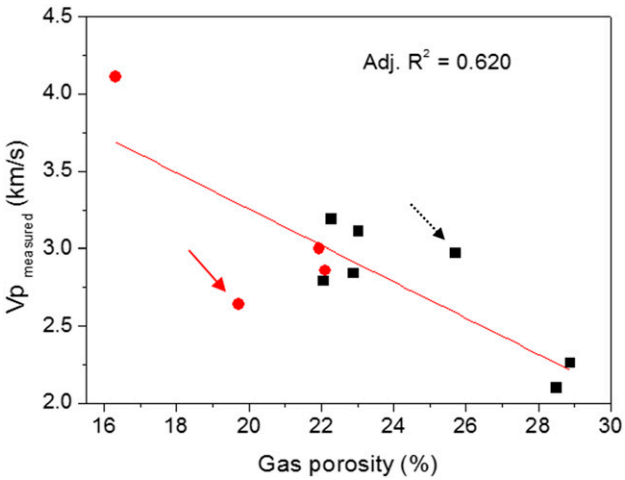

Figure 10. P-wave velocity ($V_{p\text{measured}}$) versus porosity. Cemented grainstones are represented by circles and oolitic grainstones by squares. Adj. R^2 = adjusted coefficient of determination.

or permeability with porosity and 3-D DIA parameters obtained from x-ray tomography. The following steps incorporated 3-D DIA parameters, one at a time, as a linear combination to the estimated property. All arrangements were tested, but only the higher values of adjusted R^2 are shown in Tables 5 and 6, where the p-value and statistical power are also presented.

On the first regression, six predictors were used to estimate velocity: $V_{p\text{KT}}$, γ, DomSize, τ, coordination number, and SSA. The AR and total porosity (and its micro and macro fractions) are implicit in this adjustment, because they were input parameters to the KT model. A very strong correlation is observed in this MLR; $\overline{R}^2$ improves from 0.490 to 0.962 with the combination of γ, DomSize, τ, coordination number, and SSA. In addition, an important improvement is observed when only γ, a geometrical parameter of the pore space, is incorporated into the statistical model. This strong relationship is illustrated in Figure 12.

For permeability estimation, all of the global and local parameters were used, except for porosity, which is implied in k_K. A very strong correlation is also observed in this MLR; the adjusted R^2 increases from 0.668 to 0.916 by adding only the DomSize to the model, as shown in Figure 13. By adding γ, ϕ_μ, AR, τ, and ϕ_{CT}, a slight improvement in $\overline{R}^2$ is observed.

In both cases, the p-value is always below 0.05, and the statistical power, for most of the cases, is greater than 0.8. This parameter is strongly related to the adjusted R^2, showing values not desirable for $\overline{R}^2 < 0.88$.

DISCUSSION

The influence of pore space and its geometry on acoustic properties has been explored by many authors (Rafavich et al., 1984; Anselmetti and Eberli, 1999; Assefa et al., 2003; Saleh and Castagna, 2004; Weger et al., 2009; Lima Neto et al., 2013). Although these papers consider relationships between simple pore shape, size, and acoustic properties, there is no consensus as to the influence of more complex pore types. Nevertheless, AR is always included in rock-physics models, such as KT and differential effective medium. For the complete formulation, see Mavko et al. (2009).

Table 2. Mineral Composition of the Studied Samples, Determined by X-Ray Diffraction and Rietveld Method

Samples	Calcite (wt. %)	Quartz (wt. %)	Dolomite (wt. %)	Feldspar (wt. %)	Fluorite (wt. %)
W1-01	99.71	–	0.29	–	–
W1-02	99.71	–	0.29	–	–
W1-03	95.20	2.13	0.92	1.76	–
W1-04	96.98	0.63	1.76	0.63	–
W1-05	96.47	1.46	0.52	1.55	–
W1-06	95.50	0.89	2.49	–	1.12
W1-07	96.98	1.04	1.55	0.43	–
W2-01	99.81	0.19	–	–	–
W2-02	99.37	0.64	–	–	–
W2-03	98.77	0.38	0.85	–	–
W2-04	100.00	–	–	–	–

Table 3. Petrophysical Information, Percentage of Calcite, and P-Wave Velocity of All Samples

Samples	Gas Porosity (%)	Gas Permeability (md)	Calcite (wt. %)	V_p (km/s [10^3 ft/s])
W1-01	23.03	8.95	99.71	3.11 (10.2)
W1-02	25.71	221.50	95.20	2.97 (9.7)
W1-03	22.07	32.15	96.98	2.79 (9.2)
W1-04	22.27	13.50	93.47	3.19 (10.5)
W1-05	28.89	602.30	95.56	2.26 (7.4)
W1-06	28.51	126.60	95.50	2.10 (6.9)
W1-07	22.88	9.78	96.98	2.84 (9.3)
W2-01	16.32	0.24	99.81	4.11 (13.5)
W2-02	21.94	2.02	99.37	3.00 (9.8)
W2-03	19.72	0.81	98.77	2.64 (8.7)
W2-04	22.11	1.02	100.00	2.86 (9.4)

Properties obtained from experimental measurements.
Abbreviation: V_p = P-wave velocity.

In our work, the crossplot of velocity against porosity showed significant deviations from the trend line and also a weak correlation; gas porosity explains 66% of the measured velocity (Figure 10). Geological observations alone could not explain this behavior, and there is therefore first-order evidence of multiple controls on velocity. The KT model, which is calculated from ϕ_μ and ϕ_{CT} fractions and their AR, was used for velocity (V_{pKT}) estimation. Comparison of V_{pKT} with experimental acoustic velocity also shows a poor relationship ($R^2 < 0.5$). Application of the statistical model that combines V_{pKT} and γ, a geometrical parameter redefined in this study for 3-D pores, leads to a strong correlation ($\overline{R}^2 = 0.875$). Further inclusion of DomSize in the MLR showed that more than 90% of the measured velocity is explained by the proposed model.

Weger et al. (2009) conducted a multilinear regression to assess the combined impact of multiple pore-shape parameters on V_p. They found that by taking consideration of AR and porosity the correlation was poor, with R^2 equal to 0.549 and increasing to 0.639 after inclusion of γ (defined in two dimensions), whereas the best R^2 (0.845) used these parameters, ϕ_μ, and DomSize. This study has improved on this correlation substantially by considering the geometry of the 3-D pore space. The AR of a single pore is determined by the ratio of the minor semiaxis to the major semiaxis and holds 2-D information, because the estimation of AR does not consider the

Table 4. Local and Global Parameters Obtained from Three-Dimensional Images

Samples	Macro ϕ (%)	Aspect Ratio	SSA (mm^{-1})	γ	τ	DomSize (μm)	Coordination Number	Micro ϕ (%)	% Micropores
W1-01	8.26	0.546	188	1.77	2.88	73.69	1.85	14.77	64.13
W1-02	11.52	0.544	163	1.79	2.59	76.70	1.80	14.19	55.19
W1-03	2.59	0.575	218	1.54	7.89	41.11	1.93	19.48	88.26
W1-04	4.55	0.575	189	1.65	3.47	53.22	1.57	17.72	79.57
W1-05	10.61	0.574	176	1.71	2.97	64.92	1.39	17.90	62.78
W1-06	6.49	0.575	254	1.67	2.94	46.66	1.67	22.40	77.57
W1-07	4.21	0.577	235	1.58	4.02	41.89	1.36	18.67	81.60
W2-01	1.44	0.583	721	1.54	6.08	12.20	1.99	14.88	91.18
W2-02	0.69	0.583	585	1.28	10.01	10.62	1.95	21.25	96.86
W2-03	3.01	0.551	516	2.14	6.08	19.31	1.83	16.71	84.74
W2-04	0.97	0.589	579	1.39	8.24	14.03	1.95	21.14	95.61

Abbreviations: DomSize = dominant pore size; SSA = specific surface area; γ = pore sphericity; τ = tortuosity; ϕ = porosity.

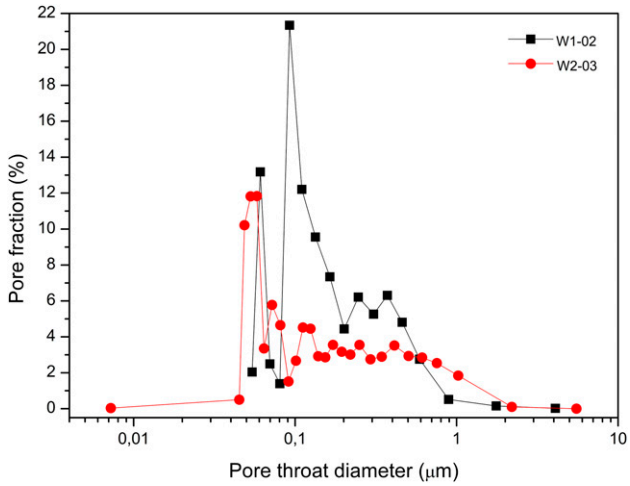

Figure 11. Pore-throat diameters and their fractions of samples W1-02 and W2-03.

third axis of the pore. Our linear regression for porosity and AR against V_p therefore resembles that published by Weger et al. (2009). In this study, however, we included a 3-D geometrical parameter, γ (which also describes the elongation of the pore), enhancing our velocity prediction substantially. In addition, our results indicate that true macropore size (DomSize), determined from 3-D data, is an important factor in the determination of acoustic velocity, because it is defined by the equivalent diameter of the pore volume. Consequently, we demonstrate that 3-D geometrical data are critical to the derivation of V_p, which is fundamentally related to pore shape and size.

Permeability prediction from porosity data in carbonate rocks is still one of the greatest challenges to carbonate petrophysical analysis. Although many clastic reservoirs show a good relationship between total porosity and permeability, such a simple relationship usually fails in carbonate rocks, and a great scattering is observed. Many studies attempt to predict permeability from porosity, SSA, and other parameters, such as sonic data. However, there is not a consensus; estimations of permeability from acoustic data are contradictory. Prasad (2003), for example, showed a correlation between permeability and P-wave based only on hydraulic units (i.e., porosity and permeability based), whereas Fabricius et al. (2007) showed that it is only possible to estimate permeability from acoustic data if the SSA of the sediment is taken into account.

Our results suggest that effective porosity and DomSize, determined from a 3-D description of the pore network, are the major controls on permeability. This is consistent with the fact that flow mainly follows large pores during fluid transport, assuming that those pores are not connected via narrow pore throats (i.e., there is not a large ratio of pore to pore throat). Although the average pore-throat diameter was not estimated for all samples and, consequently, was not an input parameter in our model, Figure 11 shows strong evidence that, for our study, larger pores (DomSize) have wider pore throats, corroborating established models from literature that correlate pore-throat diameter to permeability. Further analysis of the importance of pore to pore-throat ratio is inhibited by the ability of the software to correctly measure pore-throat diameter, and therefore it is possible that in samples with large DomSize connected by narrow pore throats DomSize would be a less important matching parameter.

Unlike the conclusions of Weger et al. (2009), ϕ_μ does not appear to be one of the most important parameters to permeability prediction within our data set. This would be expected, because most of the samples in this study are clean packstones

Table 5. Adjusted Coefficient of Determination between Measured and Estimated Velocity Using KT Model

Parameters Used to Predict P-Wave Velocity	Adjusted R^2	*P*-Value	Statistical Power
V_{pKT}	0.490	0.0098	0.63
$V_{pKT} + \gamma$	0.874	0.0001	0.76
$V_{pKT} + \gamma$ + DomSize	0.902	0.0002	0.85
$V_{pKT} + \gamma$ + DomSize + τ	0.929	0.0003	0.90
$V_{pKT} + \gamma$ + DomSize + τ + coordination number	0.944	0.0007	0.95
$V_{pKT} + \gamma$ + DomSize + τ + coordination number + SSA	0.962	0.0014	0.97

Abbreviations: DomSize = dominant pore size; R^2 = coefficient of determination; SSA = specific surface area; V_{pKT} = estimated P-wave velocity; γ = pore sphericity; τ = tortuosity.

Table 6. Adjusted Coefficient of Determination between Measured and Estimated Permeability Using Kozeny Equation

Parameters Used to Predict Permeability	Adjusted R^2	*P*-Value	Statistical Power
k_K	0.668	0.0013	0.66
k_K + DomSize	0.916	0.0001	0.98
k_K + DomSize + γ + ϕ_μ + AR + τ + ϕ_{CT}	0.948	0.010	0.99

Abbreviations: AR = aspect ratio; DomSize = dominant pore size; k_k = estimated permeability; R^2 = coefficient of determination; γ = pore sphericity; τ = tortuosity; ϕ_{CT} = macroporosity; ϕ_u = microporosity.

or grainstones in which ϕ_μ is hosted almost entirely within grains. Consequently, well-connected macropores dominate flow. This also reflects a subtle difference in terminology permitted by an improvement in the image resolution from 30 (in Weger's study) to 1.125 μm (in this study). For Weger et al. (2009), ϕ_μ included all pores that were less than 30 μm in diameter, whereas our study includes pores of 1–30 μm, which we term mesoporosity; we use the term micropores to describe all pores less than 1-μm diameter. Our results are broadly consistent with Weger et al. (2009) because of the following.

- Our data captures a proportion of the ϕ_μ that Weger et al. (2009) interpreted as controlling permeability.
- The necessarily small sample size (~2 × 2 × 2 mm [0.08 × 0.08 × 0.08 in.]) in our experiments excluded all millimeter-scale vugs that could have influenced the permeability that was measured on core plugs. However, the absence of these large pores in our 3-D pore geometrical data set does not appear to have impacted our calculated permeability.

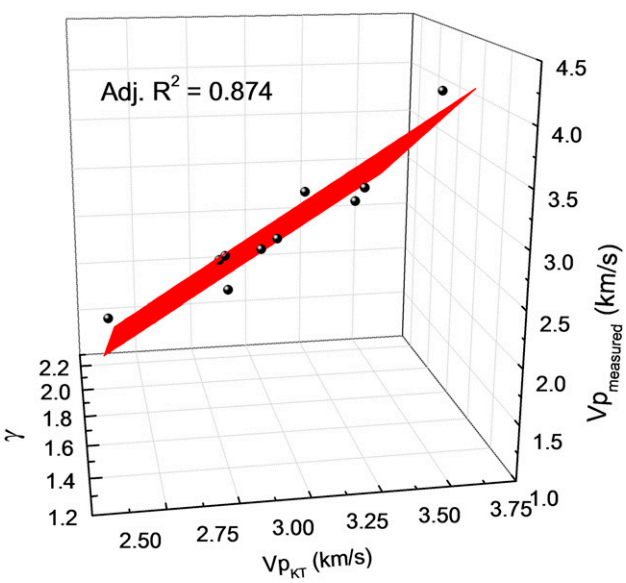

Figure 12. Three-dimensional crossplot between pore sphericity (γ), estimated velocity (V_{pKT}), and measured velocity ($V_{pmeasured}$), showing the importance of the pore shape as a controlling factor of acoustic velocity. Adj. R^2 = adjusted coefficient of determination.

In conclusion, our data support the results of previous studies that indicate that meso- and macropores (>1 μm) exert an important control on both V_p (Eberli et al., 2003; Weger et al., 2009) and permeability (Lønøy, 2006; Madonna et al., 2013). Furthermore, micropore volume and distribution will exert an important influence on hydrocarbon sweep and recovery factor, potentially leading to trapping and bypassing of hydrocarbons (e.g., Hollis et al., 2010; Harland et al., 2015).

Interestingly, our results suggest that neither coordination number nor τ are controlling factors on permeability. This is possibly related to the way that the centerline tree and τ path areas are evaluated by the visualization software. The number of nodes, necessary for coordination number estimation, is calculated by pore throats and end points, and it is not possible to determine their fractions. The τ is estimated by the path formed by centroids of each plan of a 3-D image. This prediction would improve if it were made from the centerline tree of the pore space instead of 2-D images.

CONCLUSIONS

This study presents a methodology for quantifying the local and global pore-space parameters of carbonate rocks from x-ray tomography images and incorporating their influence on permeability and acoustic properties. This study demonstrated the following.

1. X-ray microtomography is a powerful tool for the investigation and visualization of the internal structure of carbonate rocks, especially those with a grainstone texture. Local and global parameters,

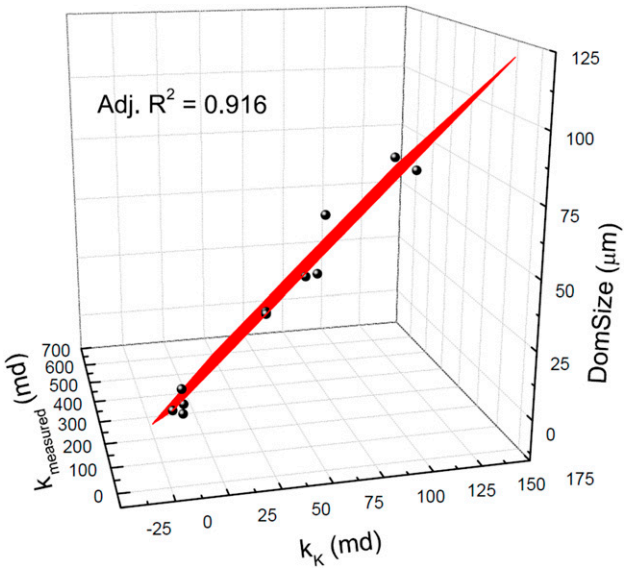

Figure 13. Three-dimensional crossplot of the relationship between dominant pore size (DomSize), estimated permeability (k_k), and measured permeability ($k_{measured}$). This figure shows the importance of the pore size as a factor controlling permeability. Adj. R^2 = adjusted coefficient of determination.

extracted from 3-D images, combined with estimated velocity or permeability, both determined from established models, are able to estimate measured velocity with $\overline{R}^2 > 0.96$ and permeability with $\overline{R}^2 > 0.94$.

2. To confidently derive velocity from the pore-space properties, it is critical to describe two geometrical parameters that most influence it: γ and DomSize. These parameters combined with $V_{p\mathrm{KT}}$ explain more than 90% of the measured velocity. Other parameters, such as SSA, have a minor influence but also improve the prediction. In sum, samples with small γ and DomSize and high SSA, coordination number, and τ present high values of velocity.
3. Porosity proved to be the main controlling factor on permeability, but a description of DomSize from a 3-D image is also fundamental to improve its estimation. The permeability estimated from Kozeny's equations, which is only porosity dependent, combined with DomSize describes more than 91% of the measured permeability; this is an impressive adjustment, because permeability prediction is still one of the greatest challenges in petrophysical analysis. By including ϕ_μ, ϕ_{CT}, AR, and τ in the model, a discrete enhancement was observed for the MLR, reaching $\overline{R}^2 = 0.948$.
4. The 3-D characterization of the shape and size of the pores was critical to the improvement of velocity and permeability predictions. A clear understanding of these controlling factors is fundamental to the petroleum industry, because these factors can affect the seismic response and log interpretation, two fundamental tools for reserves prediction and characterization.

APPENDIX: SUPPORT CROSSPLOTS

This appendix presents crossplots between measured properties and global and local parameters. In all cases, cemented grainstones are represented by circles and oolitic grainstones by squares.

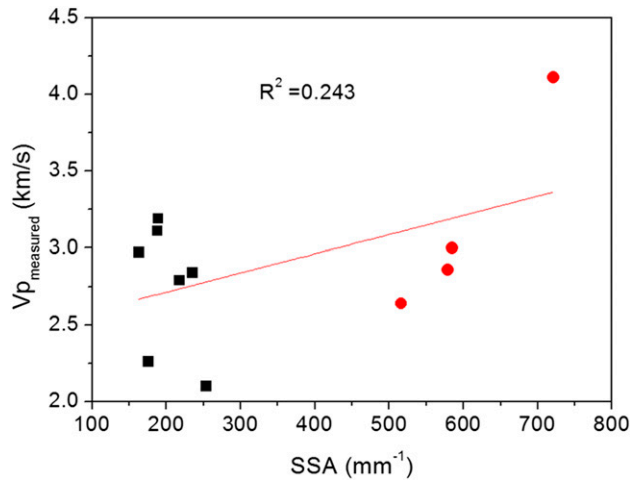

Figure 14. P-wave velocity ($V_{pmeasured}$) versus specific surface area (SSA). R^2 = coefficient of determination.

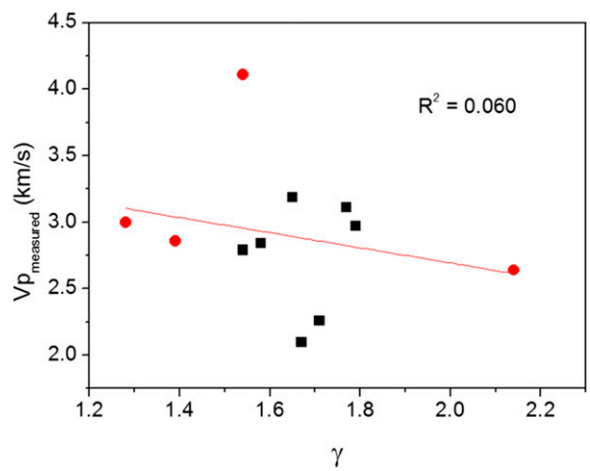

Figure 15. P-wave velocity ($V_{pmeasured}$) versus pore sphericity (γ). R^2 = coefficient of determination.

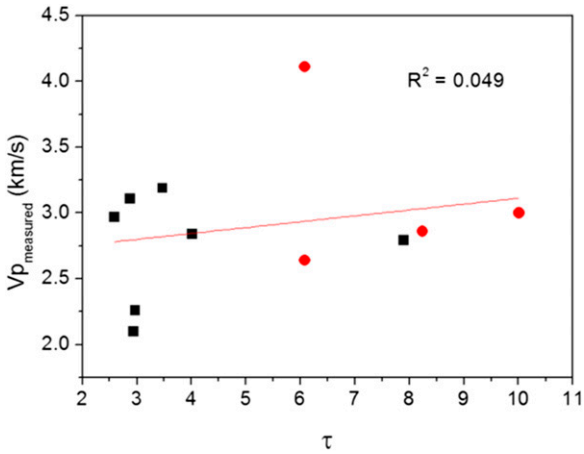

Figure 16. P-wave velocity ($V_{p\text{measured}}$) versus tortuosity (τ). R^2 = coefficient of determination.

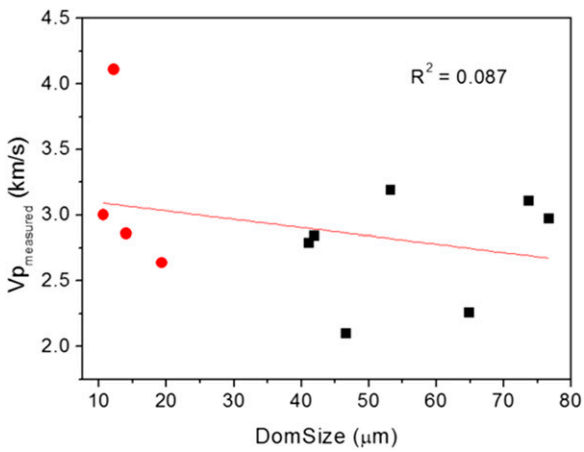

Figure 17. P-wave velocity ($V_{p\text{measured}}$) versus dominant pore size (DomSize). R^2 = coefficient of determination.

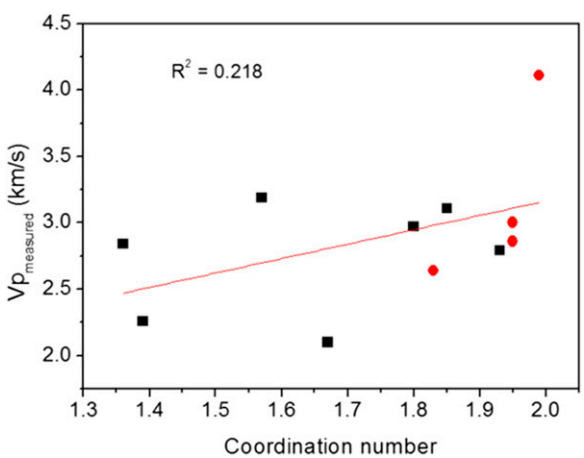

Figure 18. P-wave velocity ($V_{p\text{measured}}$) versus coordination number. R^2 = coefficient of determination.

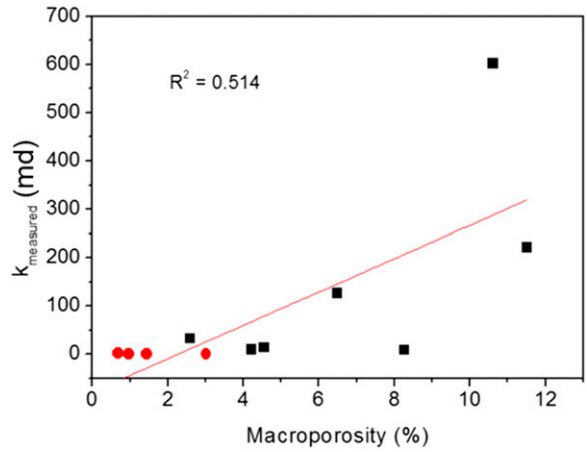

Figure 19. Gas permeability (k_{measured}) versus macroporosity. R^2 = coefficient of determination.

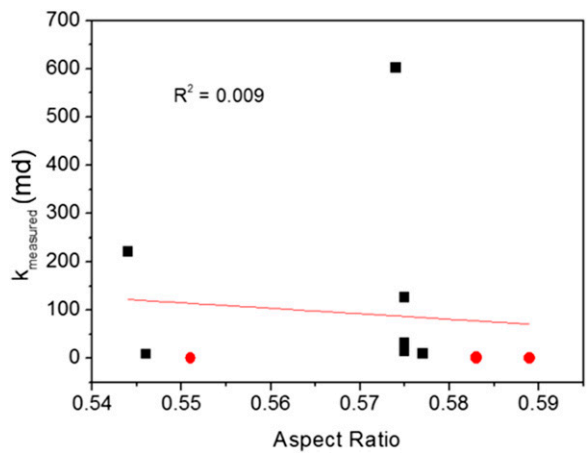

Figure 20. Gas permeability (k_{measured}) versus aspect ratio. R^2 = coefficient of determination.

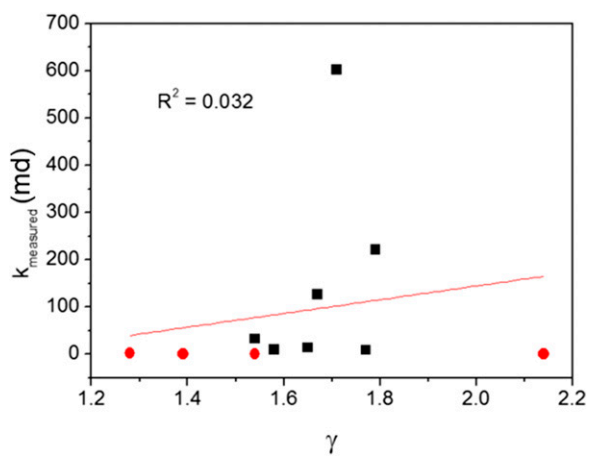

Figure 21. Gas permeability (k_{measured}) versus pore sphericity (γ). R^2 = coefficient of determination.

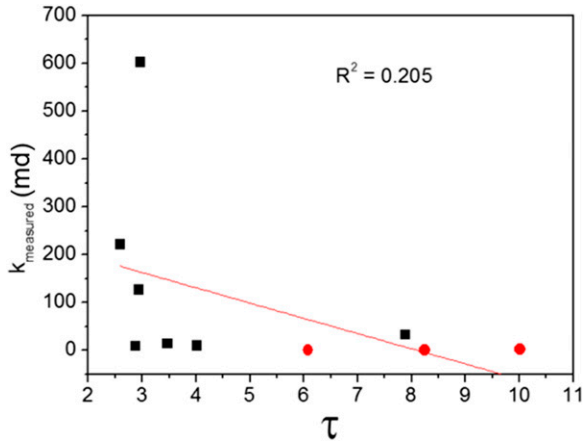

Figure 22. Gas permeability ($k_{measured}$) versus tortuosity (τ). R^2 = coefficient of determination.

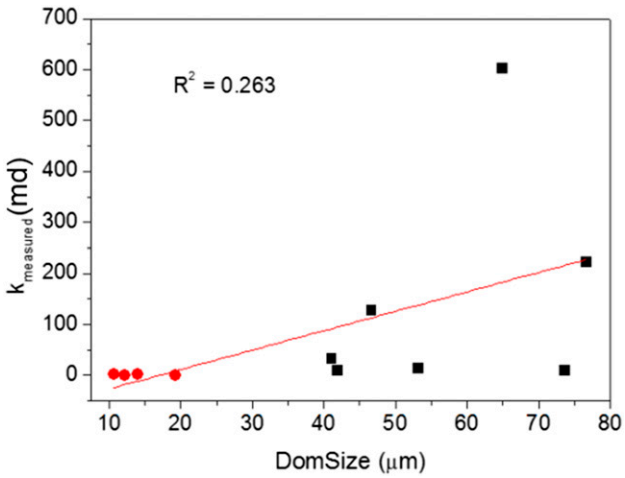

Figure 23. Gas permeability ($k_{measured}$) versus dominant pore size (DomSize). R^2 = coefficient of determination.

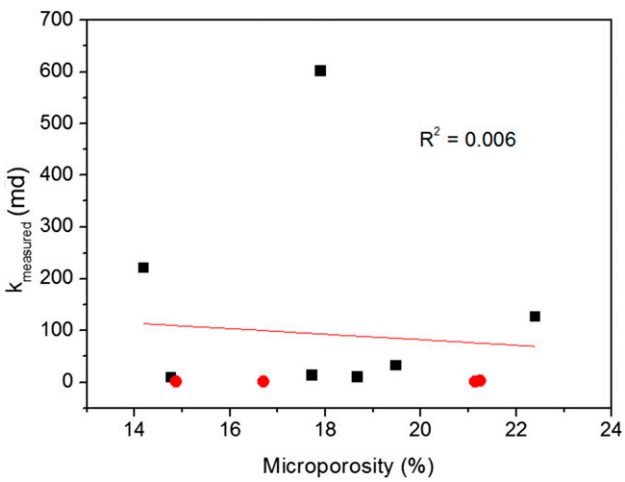

Figure 24. Gas permeability ($k_{measured}$) versus microporosity. R^2 = coefficient of determination.

REFERENCES CITED

Agência Nacional do Petróleo, 2014, Boletim de produção de petróleo e gás natural, accessed January 27, 2015, www.anp.gov.br/?dw=70566.

Ahr, W., 2008, Geology of carbonate reservoirs: The identification, description, and characterization of hydrocarbon reservoirs in carbonate rocks, 1st ed.: New York, John Wiley and Sons, 296 p.

Anselmetti, F. S., and G. P. Eberli, 1999, The velocity-deviation log: A tool to predict pore type and permeability trends in carbonate drill holes from sonic and porosity or density logs: AAPG Bulletin, v. 83, no. 3, p. 450–466.

Anselmetti, F. S., S. Luthi, and G. P. Eberli, 1998, Quantitative characterization of carbonate pore systems by digital image analysis: AAPG Bulletin, v. 82, no. 10, p. 1815–1836.

Assefa, S., C. McCann, and J. Sothcott, 2003, Velocities of compressional and shear waves in limestones: Geophysical Prospecting, v. 51, p. 1–13, doi:10.1046/j.1365-2478.2003.00349.x.

Berryman, J. G., 1980, Long-wavelength propagation in composite elastic media: Journal of the Acoustical Society of America, v. 68, p. 1809–1831, doi:10.1121/1.385171.

Brooks, G. P., and R. S. Barcikowski, 2012, The PEAR method for sample sizes in multiple linear regression: Multiple Linear Regression Viewpoints, v. 38, p. 1–16.

Bruhn, C. H., J. A. Gomes, C. D. Lucchese Jr., and P. R. Johann, 2003, Campos basin: Reservoir characterization and management—Historical overview and future challenges: Offshore Technology Conference, Houston, Texas, May 5–8, 2003, 14 p., doi:10.4043/15220-MS.

Castro, D. D., and P. L. F. Rocha, 2013, Quantitative parameters of pore types in carbonate rocks: Revista Brasileira de Geofísica, v. 31, p. 125–136.

Eberli, G. P., G. T. Baechle, F. S. Anselmetti, M. L. Incze, W. Dong, A. Tura, and G. Sparkman, 2003, Factors controlling elastic properties in carbonate sediments and rocks: Leading Edge, v. 22, p. 654–660, doi:10.1190/1.1599691.

Fabricius, I. L., G. Baechle, G. P. Eberli, and R. Weger, 2007, Estimating permeability of carbonate rocks from porosity and vp/vs: Geophysics, v. 72, p. E185–E191, doi:10.1190/1.2756081.

FEI, 2015, Avizo 3D software, accessed December 13, 2015, http://www.fei.com/software/avizo3d/.

Harland, S. R., R. A. Wood, A. Curtis, M. I. J. van Dijke, K. Stratford, Z. Jiang, W. Kallel, and K. Sorbie, 2015, Quantifying flow in variably wet microporous carbonates using object-based geological modeling and both lattice-Boltzmann and pore-network fluid flow simulations: AAPG Bulletin, v. 99, no. 10, p. 1827–1860, doi:10.1306/04231514122.

Hollis, C., V. Vahrenkamp, S. Tull, A. Mukherji, C. Taberner, and Y. Huang, 2010, Pore system characterization in heterogeneous carbonates: An alternative approach to widely used rock-typing methodologies: Marine and Petroleum Geology, v. 27, p. 772–793, doi:10.1016/j.marpetgeo.2009.12.002.

Ioannidis, M. A., and I. Chatzis, 1993, Network modelling of pore structure and transport properties of porous media: Chemical Engineering Science, v. 48, p. 951–972, doi:10.1016/0009-2509(93)80333-L.

Jivkov, A. P., C. Hollis, F. Etiese, S. A. McDonald, and P. J. Withers, 2013, A novel architecture for pore network modeling with applications to permeability of porous media: Journal of Hydrology (Amsterdam), v. 486, p. 246–258, doi:10.1016/j.jhydrol.2013.01.045.

Keys, R. G., and S. Xu, 2002, An approximation for the Xu-White velocity model: Geophysics, v. 67, p. 1406–1414, doi:10.1190/1.1512786.

Knofczynski, G. T., and D. Mundfrom, 2008, Sample sizes when using multiple linear regression for prediction: Educational and Psychological Measurement, v. 68, p. 431–442, doi:10.1177/0013164407310131.

Kozeny, J., 1927, Uber kapillare leitung des wassers im boden (aufstieg versikerung und anwendung auf die bemasserung): Akademie der Wissenschaften in Wien. Sitzungsberichte. Mathematisch-Naturwissenschaftliche Klasse. Abteilung 1, v. 136, p. 271–306.

Kuster, G. T., and M. N. Toksöz, 1974a, Velocity and attenuation of seismic waves in two-phase media: Part I. Theoretical formulations: Geophysics, v. 39, p. 587–606, doi:10.1190/1.1440450.

Kuster, G. T., and M. N. Toksöz, 1974b, Velocity and attenuation of seismic waves in two-phase media: Part II. Experimental results: Geophysics, v. 39, p. 607–618, doi:10.1190/1.1440451.

Larson, A. C., and R. B. Von Dreele, 2004, General structure analysis system: Los Alamos National Laboratory Report LAUR, p. 86–748.

Lee, M. W., 2008, Comparison of modified Biot-Gassmann theory and Kuster Toksöz theory: Reston, Virginia, US Geological Survey, Scientific Investigation Report, 14 p.

Li, H., and J. Zhang, 2010, Modulus ratio of dry rock based on differential effective medium theory: Geophysics, v. 75, p. N43–N50, doi:10.1190/1.3360312.

Lima Neto, I., R. Misságia, M. Ceia, N. Archilha, and L. Oliveira, 2013, Dual pore system evaluation of Albian grainstone carbonates from Brazil using effective elastic media theory models (abs.): Society of Exploration Geophysicists Technical Program Expanded Abstracts 2013, p. 2994–2998, doi:10.1190/segam2013-0652.1.

Lima Neto, I. A., R. M. Misságia, M. A. Ceia, N. L. Archilha, and L. C. Oliveira, 2014, Carbonate pore system evaluation using the velocity-porosity-pressure relationship, digital image analysis, and differential effective medium theory: Journal of Applied Geophysics, v. 110, p. 23–33, doi:10.1016/j.jappgeo.2014.08.013.

Lønøy, A., 2006, Making sense of carbonate pore systems: AAPG Bulletin, v. 90, no. 9, p. 1381–1405, doi:10.1306/03130605104.

Lucia, F. J., 2007, Carbonate reservoir characterization: An integral approach, 2nd ed.: Heidelberg, Germany, Springer Science, 337 p.

Madonna, C., B. Quintal, M. Frehner, B. S. G. Almqvist, N. Tisato, M. Pistone, F. Marone, and E. H. Saenger, 2013, Synchrotron-based x-ray tomographic microscopy for rock physics investigations: Geophysics, v. 78, p. D53–D64, doi:10.1190/geo2012-0113.1.

Matthews, G. P., and M. C. Spearing, 1992, Measurements and modeling of diffusion, porosity and other pore level characteristics of sandstone: Marine and Petroleum Geology, v. 9, p. 146–154, doi:10.1016/0264-8172(92)90087-U.

Mavko, G., T. Mukerji, and J. Dvorkin, 2009, The rock physics handbook: Tools for seismic analysis of porous media, 2nd ed.: New York, Cambridge University Press, 525 p., doi:10.1017/CBO9780511626753.

Miller, D. E., and T. J. Kunce, 1973, Prediction and statistical overkill revisited: Measurement and Evaluation in Guidance, v. 6, p. 157–163.

Mortensen, J., F. Engdtrom, and I. Lind, 1998, The relation among porosity, permeability, and specific surface of chalk from the Gorm field, Danish North Sea: SPE Reservoir Evaluation and Engineering, v. 1, no. 3, SPE-31062-PA, p. 245–251, doi:10.2118/31062-PA.

Pedhazur, E. J., and L. P. Schmelkin, 1991, Measurement, design, and analysis: An integrated approach: New York, Psychology Press, 840 p.

Prasad, M., 2003, Velocity-permeability relations within hydraulic units: Geophysics, v. 68, p. 108–117, doi:10.1190/1.1543198.

Pratson, L. F., A. Stroujkova, D. Herrick, F. Boadu, and P. Malin, 2003, Predicting seismic velocity and other rock properties from clay content only: Geophysics, v. 68, p. 1847–1856, doi:10.1190/1.1635037.

Rafavich, F., C. H. St. C. Kendall, and T. P. Tood, 1984, The relationship between acoustic proprieties and the petrographic character of carbonate rocks: Geophysics, v. 49, p. 1622–1636, doi:10.1190/1.1441570.

Raoof, A., and S. M. Hassanizadeh, 2012, A new formulation for pore-network modeling of two-phase flow: Water Resources Research, v. 48, p. 1–13, doi:10.1029/2010WR010180.

Raymer, L. L., E. R. Hunt, and J. S. Gardner, 1980, An improved sonic transit time-to-porosity transform: Society of Petrophysicists and Well Log Analysts 21st Annual Logging Symposium, Lafayette, Louisiana, July 8–11, 1980, p. 1–12.

Reeves, P. C., and M. A. Celia, 1996, A functional relationship between capillary pressure, saturation, and interfacial area as revealed by a pore-scale network model: Water Resources Research, v. 32, p. 2345–2358, doi:10.1029/96WR01105.

Rietveld, H. M., 1969, A profile refinement method for nuclear and magnetic structures: Journal of Applied Crystallography, v. 2, p. 65–71, doi:10.1107/S0021889869006558.

Saleh, A. A., and J. P. Castagna, 2004, Revisiting the Wyllie time average equation in the case of near spherical pores: Geophysics, v. 69, p. 45–55, doi:10.1190/1.1649374.

Sayers, C. M., 2008, The elastic properties of carbonates: Leading Edge, v. 27, p. 1020–1024, doi:10.1190/1.2967555.

Wang, H., and S. Z. Sun, 2010, A full-frequency band Kuster-Toksöz model and its application in velocity dispersion

analysis: Society of Exploration Geophysicists Annual Meeting, Denver, Colorado, October 17–22, 2010, 5 p.

Weger, R. J., G. P. Eberli, G. T. Baechle, J. L. Massaferro, and Y. Sun, 2009, Quantification of pore structure and its effect on sonic velocity and permeability in carbonates: AAPG Bulletin, v. 93, no. 10, p. 1297–1317, doi:10.1306/05270909001.

Wu, T. T., 1966, The effect of inclusion shape on the elastic moduli of a two-phase material: International Journal of Solids and Structures, v. 2, p. 1–8, doi:10.1016/0020-7683(66)90002-3.

Wyllie, M. R. J., A. R. Gregory, and G. H. F. Gardner, 1958, An experimental investigation of factors affecting elastic wave velocities in porous media: Geophysics, v. 23, p. 459–493, doi:10.1190/1.1438493.

Xu, S., and R. E. White, 1995, A new velocity model for clay-sand mixtures: Geophysical Prospecting, v. 43, p. 91–118, doi:10.1111/j.1365-2478.1995.tb00126.x.

Zhang, Z., and R. R. Stewart, 2008, Rock physics models for cracked media: CREWES Research Report, Calgary, Alberta, Canada, Consortium for Research in Elastic Wave Exploration Seismology, v. 20, 16 p.